

Gold Nanocage-Based Multifunctional Nanosensitizers for Programmed Photothermal / Radiation/Chemical Coordinated Therapy Guided by FL/MR/PA Multimodal Imaging

Xinni Pan¹, Yi Lu², Shanshan Fan¹, Hao Tang², Haisong Tan³, Cheng Cao², Yingsheng Cheng¹, Yanlei Liu²

¹Department of Radiology, Shanghai Sixth People's Hospital Affiliated to Shanghai Jiao Tong University School of Medicine, Shanghai, People's Republic of China; ²Department of Instrument Science and Engineering, Institute of Nano Biomedicine and Engineering, Shanghai Engineering Research Centre for Intelligent Diagnosis and Treatment Instrument, School of Electronic Information and Electrical Engineering, Shanghai Jiao Tong University, Shanghai, People's Republic of China; ³Department of Urology, Shanghai Ninth People's Hospital, Shanghai Jiao Tong University School of Medicine, Shanghai, People's Republic of China

Correspondence: Yingsheng Cheng, Department of Radiology, Shanghai Sixth People's Hospital Affiliated to Shanghai Jiao Tong University School of Medicine, Shanghai, 200235, People's Republic of China, Tel +86-021-38297858, Email chengyingsheng@hotmail.com; Yanlei Liu, Institute of Nano Biomedicine and Engineering, Shanghai Engineering Research Centre for Intelligent Diagnosis and Treatment Instrument, Department of Instrument Science and Engineering, School of Electronic Information and Electrical Engineering, Shanghai Jiao Tong University, 800 Dongchuan Road, Shanghai, 200240, People's Republic of China, Tel +86-18721788078, Email liuyanlei@sjtu.edu.cn

Background: Radiotherapy is one of the main clinical methods for the treatment of malignant tumors at present. However, its application is limited by the radiation resistance of some tumor cells and the irradiation damage to the surrounding normal tissues, and the limitation of radiotherapy dose also affects the therapeutic effect. Therefore, developing diagnostic and therapeutic agents with imaging and radiosensitizing functions is urgently needed to improve the accuracy and efficacy of radiotherapy.

Materials and Strategy: Herein, we synthesized multifunctional nanotheranostic FRNPs nanoparticles based on gold nanocages (GNCs) and MnO₂ for magnetic resonance (MR)/photoacoustic (PA) imaging and combined photothermal, radiosensitive and chemical therapy. A programmed therapy strategy based on FRNPs is proposed. First, photothermal therapy is applied to ablate large tumors and increase the sensitivity of the tumor tissue to radiotherapy, then X-ray radiation is performed to further reduce the tumor size, and finally chemotherapeutic agents are used to eliminate smaller residual tumors and distant metastases.

Results: As revealed by fluorescence, MR and PA imaging, FRNPs achieved efficient aggregation and retention at tumor sites of mice after intravenous injection. In vivo studies have shown that the programmed treatment of FRNPs-injected nude mice which were exposed to X-ray after 808 laser irradiation achieved the greatest inhibition of tumor growth compared with other treatment groups. Moreover, no obvious systemic toxicity was observed in all groups of mice, indicating the good biocompatibility of FRNPs and the safety of the treatment scheme.

Conclusion: To sum up, our work not only showed a new radiosensitizer, but also provided a promising theranostic strategy for cancer treatment.

Keywords: gold nanoparticles, MnO₂, radiosensitizing, multimodal imaging, cancer therapy

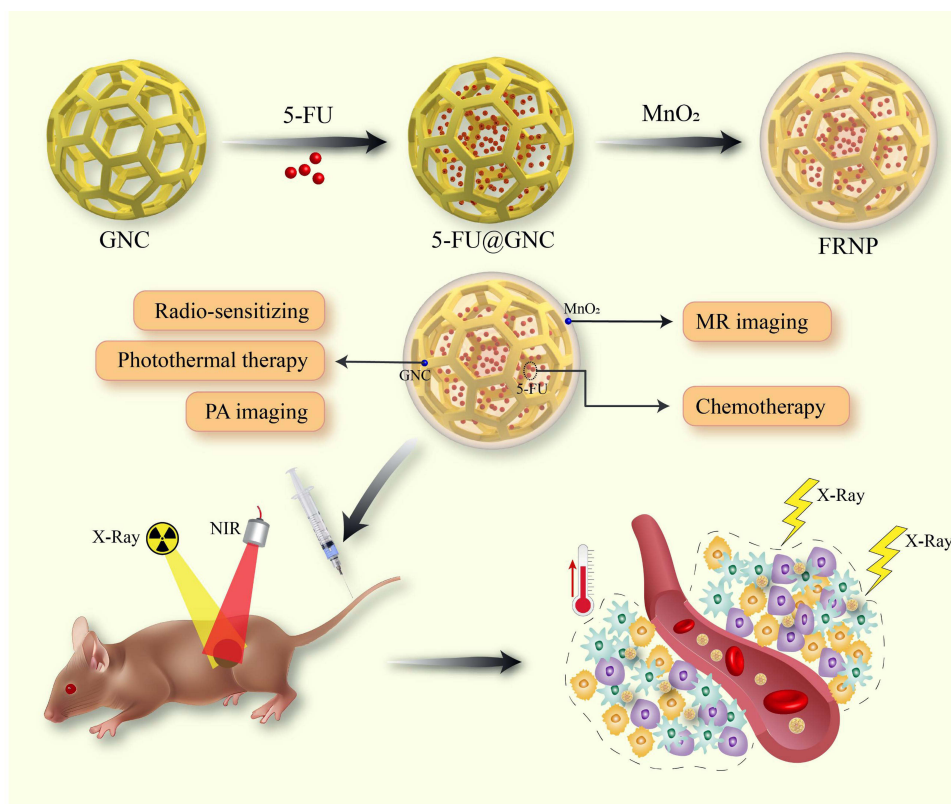
Introduction

Worldwide, Esophageal cancer (EC) is one of the most common gastrointestinal malignancies and has the sixth highest cancer mortality. An estimated 604,100 new oesophageal cancer cases and 544,076 deaths occurred in 2020 worldwide.¹ The most common histopathologic types of oesophageal cancer are oesophageal squamous cell carcinoma (OSCC) and adenocarcinoma (OAC) which differ in biology and epidemiology.² Radiotherapy (RT) is an important tool in the multidisciplinary management of EC, which has been widely used for palliative, adjuvant, and curative therapy.³ The

basic principle of radiotherapy is that high-energy ionizing radiation (such as X-rays and gamma rays) directly interacts with DNA to cause damage to the DNA, such as strand breaks, point mutation, and aberrant DNA cross-linking or indirectly react with water molecules to produce reactive oxygen radicals, which damage DNA and other cell components, and thus induce cell apoptosis and necrosis. Remarkably, high-energy radiation could cause fatal damage to cancer cells without depth restriction.^{4,5} However, there are some intrinsic shortcomings of traditional radiotherapy that limit its long-term application. First, the utilization of RT to kill cancer cells leads to inevitable injuries to normal tissues and organs around the tumor and thus causing serious side effects to body.⁶⁻⁸ Moreover, the hypoxic nature inside the tumor microenvironment (TME) may result in insensitivity to ionizing radiation, which leads to radioresistance and failure of RT.^{9,10} Currently, how to cope with the radiation resistance of cancerous cells is still a great challenge to radiation oncologist. It is unwise to exert excessive radiation dosages in the therapy process to obtain the desirable radiotherapeutic efficacy, as blindly increasing the radiation dosage can not increase the efficacy of radiotherapy but aggravate the injury of normal tissue.^{11,12} The employment of radiosensitizers may be a proper strategy to overcome the radiation resistance and achieve relatively safe and low-dosed radiation therapeutics.¹³

The combination treatment is also regarded as an effective solution to optimize therapeutic effect.¹⁴ Induced by PTT, an appropriate hyperthermia level could accelerate blood circulation and subsequently improve the oxygen content in the tumor, which would enhance the sensitivity of hypoxic cancerous cells to RT.^{14,15} As a simple, safe, and minimally invasive tumor therapeutic method, photothermal therapy (PTT) utilizes photothermal transduction agents (PTAs) that can absorb NIR light to convert the photo energy into thermal energy, resulting in thermal ablation of cancerous cells and tissues exposed to laser irradiation.^{6,16} However, limited by the tissue penetration depth of laser, deep cancer cells, and tissues are usually difficult to be eradicated.¹⁷ Unlike that of photothermal therapy, radiotherapy can effectively kill tumor cells regardless of tissue depth. Therefore, the combination of PTT with RT would obtain enhanced therapeutic efficiency than the two strategies respectively due to the fact that the advantages of both could be taken of, while the shortcomings of either could be avoided. Based on this, it is urgently desirable to develop promising PTT/RT agents that own excellent photothermal conversion performance as well as radiosensitizing effect. To date, a number of different nanomaterials have been widely explored as PTT/RT agents in response to the needs above. For example, Wang et al demonstrated MoS₂ quantum dots covered with polyaniline possessing a remarkable PTT/RT synergistic effect for cancer treatment.¹⁸ Yin et al synthesized ultrasmall zirconium carbide (ZrC) nanodots with high near-infrared absorption and strong photon attenuation for synergistic PTT-RT treatment.¹⁹ Zhang et al prepared Cu_xS/Au nanocomposites for the combination of PTT and RT, achieving remarkable synergistic therapeutic effects.²⁰ In recent years, nanoscale metal-organic framework (NMOF) and bismuth nanomaterials which possess efficient photothermal conversion capability and radiosensitization properties have been utilized as a multifunctional nanomedicine platform for PTT and RT.²¹⁻²⁵ In addition, the integration of photothermal nanomaterials with radionuclide to achieve synergistic PTT and brachytherapy (BT) treatment has also been reported.²⁶⁻²⁸ Gold nanoparticles (AuNPs) have attracted much attention in the field of biomedicine owing to their superior physicochemical properties and fine biocompatibility.^{3,29-37} AuNPs have been utilized as photothermal agents due to their good optical absorption properties and excellent photothermal transfer ability.³⁸⁻⁴⁰ In addition, AuNPs, as high Z nanomaterials, which can absorb more photons, have an obvious energy deposition effect on X-ray radiation. After being administrated via intravenous injection and accumulating around tumor tissues, AuNPs can increase the intracellular radiation energy deposition and enhance the effect of radiation on cancer cells killing and tumor tissue destruction.^{4,41-43} In the aspect of imaging, AuNPs have also been a kind of ideal contrast reagents for photoacoustic (PA) imaging due to their tunable optical characteristics.^{44,45} The potential biocompatibility and easier functionalization of AuNPs make them appropriate theranostic agents for image-guided synergistic therapy.

As a novel and easily synthesized inorganic nanoparticle with high biosafety, manganese dioxide (MnO₂) has been taken account of by many researchers in the construction of nanomedicine systems.⁴⁶⁻⁴⁹ It has a unique ability to modulate tumor microenvironment (TEM) which is generally characterized by severe hypoxia, overproduced hydrogen peroxide (H₂O₂), low PH value and high levels of glutathione (GSH).⁵⁰ MnO₂ has relatively strong catalytic activity under the weakly acidic tumor microenvironment, which can trigger the decomposition of tumor endogenous excess hydrogen peroxide (H₂O₂) into water and oxygen, thus improving the low level of oxygen in TEM as well as sensitizing the radiotherapy-resistant tumor cells.⁵¹ At the same time, MnO₂ is reduced to Mn²⁺, which can be used as a contrast agent in magnetic resonance imaging, helping to trace drugs and image tumors.⁵² Meanwhile, free Mn²⁺ will soon be metabolized from the body by excreting from the kidney without causing



Scheme 1 Schematic illustration of design and synthesis of FRNPs; detailed processes of FRNPs for tumor therapy.

long-term toxic effects.⁴⁶ We speculated that the combination of gold nanoparticles and MnO₂ could serve as the MR/PA imaging agent, PTA, and radiosensitizer to realize MR/PA imaging-guided PTT/RT combined therapy.

In this work, we have successfully prepared 5-FU@GNC@MnO₂ Ferrero Rocher-type nanoparticles (FRNPs). Gold nanocages (GNCs) and manganese dioxide (MnO₂) are two noteworthy kinds of intrinsic theranostic nanoparticles. Since EC usually forms micrometastasis in the early stages and chemotherapy is normally the first choice of treatment of metastases.⁵³ Thus, cytotoxic drugs 5-fluorouracil were added in the nanoplatform to eliminate smaller residual tumors and distant metastatic tumor cells. In general, gold nanocages (GNCs) were employed as carriers, in which chemotherapy drugs were loaded. After that, manganese dioxide (MnO₂) nanoparticles were formed outside the GNCs as a blocking agent in case of the leakage of drugs in it. Finally, the nanoparticles were successfully fabricated. In this system, MnO₂ afforded catalase(CAT)-like activity and T1-weighted MR contrast, while gold nanocages endowed the nanoplatform with excellent photoconversion performance and energy deposition effect under NIR laser excitation and X-ray irradiation, thus enhancing PTT as well as RT and achieving great PA imaging (Scheme 1). We found that tumor growth could be remarkably inhibited by means of adopting FRNPs to achieve a programmed PTT/RT/CT therapy under Fluorescence/MR/PA imaging in tumor bearing mice. Furthermore, no obvious systemic toxicity was detected by histological analysis in major organs after i.v. administration within 14 days, revealing good biocompatibility. Those results demonstrated that the synthesized FRNPs might open new avenues for clinical tumorous nanotheranostics with precise diagnosis and imaging-guided complex therapy.

Materials and Methods

Material

Chloroauric acid (HAuCl₄), ethylene glycol (EG), sodium sulfide (Na₂S), polyvinylpyrrolidone (PVP), silver nitrate (AgNO₃), acetone (AC), PAH (MW, 17,500) were purchased from Aladdin Biochemical Technology Co. Ltd. (Shanghai, China). Potassium permanganate (KMnO₄, 99%) was purchased from Sinopharm Chemical Reagent Co. Ltd (China). 5-FU was obtained from Sigma-Aldrich. Dimethyl sulfoxide (99.7%) was obtained from Shanghai Lingfeng Chemical Reagent Co. Ltd. All cell culture products were supplied by GIBCO (Grand Island, NY, USA). The Cell Counting Kit-8 (CCK-8) was obtained from Dojindo

Molecular Technologies (Japan). Crystal violet staining solution was supplied by Shanghai Yuanye Bio-Technology Co. Ltd. Calcein-AM/PI double staining kit was supplied by Beyotime Biotechnology. Annexin V-FITC/PI apoptosis detection kit was supplied by Yeasen Co. (Shanghai, China). Cy7-PEG-SH (MW, 5000) was obtained from MeloPEG Technology Co. Ltd. Anti-Human Phospho-H₂AX (S139) Alexa Fluor 488 mouse mAb was supplied by eBioscience (USA). Deionized water (18.2 MΩ cm⁻¹) was generated using a Millipore Milli-Q purification system and used in all experiments. All chemical reagents were of analytical grade and used without any additional treatment and purification.

Preparation of Gold Nanocages (GNCs)

The gold nanocages (GNCs) were synthesized based on a galvanic replacement reaction between silver nanocubes and chloroauric acid (HAuCl₄) according to previous reports with some modification.^{54,55} To obtain the Ag nanocubes, 25 mL of ethylene glycol (EG) was heated to 150 °C under magnetic stirring in oil bath for 1h, and 350 μL of 3 mM Na₂S solution (in EG) was quickly added into the heated solution. After 8 min, 7.5 mL of PVP (20 mg/mL in EG and 2.5 mL of silver nitrate (282 mM in EG) were sequentially injected into the reaction mixture. The mixture was further stirred at 150 °C for 20 minutes, after which the reaction bottle was removed into an ice-cold water bath to quench the reaction. Then the reaction solution was diluted with 70 mL acetone, centrifuged at 2000 g for 30 min to spin down the product. The product was then washed with water three times to remove the remaining EG and PVP, and the precipitate was collected and stored in 4 °C for further use. For synthesis of GNCs, 2 mL of 0.1 mM Ag nanocubes were added into 50 mL of 9 mM PVP solution under magnetic stirring and then heated to 70 °C. Meanwhile, 0.1 mM HAuCl₄ solution was injected through a syringe pump at a rate of 1 mL/min, and absorption spectrometry was used to monitor the progress. The injection was stopped until the appropriate SPR peak appeared. The final products were concentrated and washed and finally dispersed for further applications.

Preparation of 5-FU@GNC

In detail, 3 mL of 0.1 mg/mL as-prepared gold nanocages (GNCs) solution was transferred into a clean glass vial, and then 100 μL of 5-fluorouracil (1 mg/mL) were added. After moderate shaking in the dark for 24 h at room temperature, 5-FU@GNC was collected by centrifuging the suspension at 16,800 g for 20 min and washed three times with deionized water. The concentration of 5-FU loaded into the GNCs was calculated using UV-vis spectroscopy. Following previously reported method,⁴⁵ The LR and EE of 5-FU were calculated as follows:

$$LR(100\%) = \frac{(\text{weight of 5 - FU loaded})}{(\text{total weight of nanoparticles})} \times 100\%$$

$$EE(100\%) = \frac{(\text{weight of 5 - FU loaded})}{(\text{total weight of 5 - FU added initially})} \times 100\%$$

Preparation of 5-FU@GNC@MnO₂

5-FU@GNC@MnO₂ nanoparticles were synthesized according to the method reported by Liu with slight modifications.⁵⁶ Briefly, the above formed 5-FU@GNC was gently dispersed in 3 mL of deionized water in a reaction vial, after which KMnO₄ (2 μL, 10 mg/mL) was slowly added under moderate stirring and the violet dispersion was continuously stirred for 2h at room temperature. Next, PAH (200 μL, 23.6 mg/mL) was dropped in the mixture. As soon as PAH was added, the color of the solution changed to brown from violet within a short period of time. After reaction for 30 min, the suspension was centrifuged at 12000g for 30 min. After removing supernatant, the precipitate was resuspended in 2 mL of deionized water. Then the prepared 5-FU@GNC@MnO₂ nanoparticles (FRNPs) were stored at 4 °C for further use.

Characterization

The morphology and structure of synthesized FRNPs were characterized by transmission electron microscopy (TEM, Tecnai G2 spirit Biotwin, USA). The chemical state was analyzed by X-ray photoelectron spectroscopy (XPS, AXIS Ultra DLD, Japan). The UV-vis spectra was collected using a UV-vis spectrophotometer (Varian Inc., Palo Alto, CA,

USA) at a wavelength range of 200–1100 nm. Hydrodynamic size and zeta potential were measured by a particle size zeta potential analyzer (Nicom 380 DLS, USA). The T1 relaxation times of different concentrations of nanoparticles were investigated using a 0.5 T MRI scanner (MesoMR23-060H-I; Shanghai Niumag Corporation, China).

Degradation and Drug Release Experiments at Different pH

The release of 5-FU in PBS was determined by absorption spectrometry using a UV-Vis spectrometer. FRNPs were dispersed in deionized water at different pH values, incubated at pH 7.4, 6.5 and 5.0 respectively. At predetermined time points, 1 mL dispersion was collected and put into a ultrafiltration tube (interception molecular weight: 7 kDa). In addition, add another 1 mL deionized water to the reaction solution and keep the total volume unchanged. After centrifugation, the concentration of 5-FU in the supernatant was calculated by measuring the absorbance (260 nm) of the supernatant, thus the content of 5-FU released from FRNPs to buffer solution was obtained.

In vitro Photothermal Properties

The photothermal performance of FRNPs was estimated using a hand-held 808 NIR laser, which power density was maintained at 1.5 W/cm² in all tests. The volume of FRNPs aqueous dispersion in each test was 200 μL. Temperature changes were recorded with the help of a thermal imaging camera and quantified by testo IRSoft. For concentration-dependent photothermal performance, FRNPs were diluted to a series of solutions with various concentrations (25, 50, and 100 μg/mL) followed by exposing to laser for 150 s and pure PBS was used as a control. To assess the photothermal stability, laser on/off cycle assays were carried out. In detail, FRNPs aqueous dispersion with a concentration of 100 μg/mL was irradiated by laser for 180 s (laser on), and naturally cooled down without irradiation for another 180 s (laser off). Such on/off cycles were repeated 6 times. Following previously reported method,⁵⁷ the photothermal conversion efficiency was calculated according to Eqs below:

$$\eta = \frac{hA(\Delta T_{\max} - \Delta T_{\max, \text{PBS}})}{I(1 - 10^{-A_{\lambda}})}$$

where η is the photothermal conversion efficiency, h is the heat-transfer coefficient, A is the surface area of container, T_{\max} is the maximum temperature of FRNPs aqueous dispersion, $T_{\max, \text{PBS}}$ is the maximum temperature of PBS, I is the laser power, A_{λ} is the absorbance of FRNPs aqueous dispersion at the wavelength of 808 nm.

Cell Culture

Human esophageal cancer ECA109 cell line was obtained from the Cell Bank of the Chinese Academy of Sciences. All cell culture products were supplied by GIBCO (Grand Island, NY, USA). The cells were cultured in RPMI-1640 medium containing 10% fetal bovine serum (FBS) and 1% penicillin/streptomycin and cultivated in a humidified atmosphere at 37 °C with 5% CO₂. Cells in the logarithmic growth phase were used in vitro and in vivo experiments.

Cytotoxicity Assay

The cytotoxicity of FRNPs against ECA 109 cells was assessed by CCK-8 assay. In detail, ECA109 cells were seeded in a 96-well plate at a density of 5000 cells per well and cultured for 24 h until approximately 80% confluency. Then cells were cocultured with culture media alone or different concentrations (25, 50, 100, 150 and 200 μg/mL) of FRNPs for another 24, 48, 72 h. Thereafter, the culture media was removed and the cells were washed three times with sterile PBS (pH 7.4). Sequently, 100 μL of Cell culture medium containing CCK8 test solution was added to the wells. After further incubation for 1 h, the absorbance of the plate was scanned at a wavelength of 450 nm using a microplate reader to evaluate the relative cell viability. Each experiment was performed in triplicate.

Cellular Uptake

Transmission Electron Microscopy (TEM) was employed to observe the cellular uptake and subcellular distribution of FRNPs. ECA 109 cells were seeded in a 100×15 mm cell culture dish and incubated for 18 h to allow for cell adherence. Then cell culture medium was replaced with freshly prepared FRNPs diluted in RPMI-1640 medium and the ECA 109 cells were

incubated for additional 24 h at 37 °C in a humidified incubator under 5% CO₂ atmosphere. Afterward, the cells were digested and collected by centrifugation. The supernatant was discarded, while the precipitate was fixed with 2.5% glutaraldehyde. Then the precipitate was washed three times with 0.1 M Phosphate buffer (pH 7.4), pre-embedded, post-fixed with 1% osmium tetroxide at room temperature and dehydrated by gradient ethanol. Finally, the samples were embedded in resin. Ultrathin sections (60–80 nm) of fixed ECA 109 were prepared by an ultramicrotome, fished out onto the 150 meshes copper grids, and stained doubly with 2% uranium acetate and 2.6% lead citrate. The prepared samples were then observed and taken images using bio-TEM (HT7800 Hitachi, Japan). In the quantitative study of cellular uptake, the FRNPs was labelled by Cy7, a red fluorescent probe. ECA 109 cells were seeded at a density of 1.0×10^5 in 12-well plates and incubated at 37 °C for 24 h. The medium was then replaced by fresh 1640 medium alone or freshly prepared Cy7-FRNPs solution in 1640 medium (100 µg/mL). The treated cells were incubated for a further 24 h. Subsequently, the cells were digested from the plate with trypsin-EDTA. The red fluorescence signal inside cells from Cy7 labeled FRNPs was quantified via a flow cytometer.

Clonogenic Assay

To evaluate the effects of respective treatment and radiosensitizing ability of FRNPs, different numbers of ECA 109 cells (300, 600, 1200, 3000 and 3000) were seeded in 6-well plates according to the radiation doses of 0, 2, 4, 6, and 8 Gy for 24 h, the cells were divided into eight groups which would undergo different treatments: (a) control, (b) NIR only, (c) FRNPs only, (d) FRNPs + NIR, (e) X-ray only, (f) NIR + X-ray, (g) FRNPs + X-ray, and (h) FRNPs + NIR + X-ray. Firstly, the cells were incubated with the medium alone or FRNPs for 24 h. After 24 h coincubation, FRNPs in medium was removed and washed twice with PBS buffer, and then replaced with fresh culture medium. Thereafter, groups (b) and (d) were irradiated with an 808 nm NIR laser for 5 min (1.5 W/cm^2), groups (e) and (g) were exposed to different doses (0, 2, 4, 6, and 8 Gy) of X-ray by a linear accelerator (RS2000, Rad Source, USA). Groups (f) and (h) were first treated with 808 nm NIR laser irradiation for 5 min (1.5 W/cm^2) and then received the administration of X-ray with different doses (0, 2, 4, 6, and 8 Gy). After different treatments, the cells were continuously cultured for additional 7–10 days to allow for colonies formation. During the process, the culture medium was refreshed every 3 days. Subsequently, the cells were fixed with 4% paraformaldehyde, stained with crystal violet and kept in air until dry. The colonies with more than 50 cells were counted and the colony formation rate was calculated using the equation: colony formation rate = (number of colonies/number of seed cells) × 100%. There are three replicates in each group.

Calculation of Sensitization Enhancement Ratio (SER)

The cell survival fraction of each group was calculated by the colony formation rate of the respective treatment groups to that of the control group. The classical multitarget single-hit model was applied to perform nonlinear fitting for the cell survival fraction of each group using matlab R2019b software. The cell survival curve was also fitted using a multitarget single-hit model ($S = 1 - (1 - e^{-(D/D_0)^N})^N$), where S is the surviving fraction and D is the radiation dose. The value of D_0 was estimated from the fitting, and the SER was determined by the radiation dose that led to a 50% survival of the cells.

Immunofluorescence Assay for Phosphorylated Ser 139 on Histone H₂AX (γ -H₂AX)

After different treatments for 1 h, cells were rinsed three times with cold PBS, fixed with 4% glutaraldehyde for 10 min, and permeabilized with 1% Triton X-100. Afterward, cells were blocked with a blocking buffer (2% BSA in PBS solution) for 60 min to avoid nonspecific protein adsorption. Next the cells were incubated overnight at 4 °C with Anti-Human Phospho-H2AX (S139) Alexa Fluor 488 mouse mAb (eBioscience, USA) at 1:200 dilution in 0.1% BSA. The nuclei were stained with DAPI for 5 min at room temperature. The formation of γ -H₂AX foci at DNA double-strand breaks sites was observed and imaged using confocal laser scanning microscope (CLSM) (TCS SP8 STED 3X; Leica; Germany). Foci were counted automatically using ImageJ software and the average number of γ -H₂AX foci was calculated for at least 50 nuclei.

Live/Dead Staining

ECA 109 cells were cultured in 48-well plates overnight, then 200 µL of FRNPs or PBS was added for another 24 h co-incubation. Some wells were then exposed to an 808 nm NIR laser (1.5 W/cm^2 , 5 min) and/or X-rays under a dose of 6

Gy. After 24 h incubation, ECA 109 cells were stained with a live/dead viability/cytotoxicity kit according to the manufacturer's instructions. The live (green) and dead (red) cells were distinguished and photographed with a confocal laser scanning microscope (CLSM) (TCS SP8 STED 3X; Leica; Germany).

Apoptosis Assay

To compare the apoptosis-inducing capabilities between groups with different treatment, the Annexin V-FITC/PI apoptosis detection assay was carried out. In brief, ECA 109 cells were cultivated in 6-well plates overnight and treated with various methods. After 24 h treatment, ECA 109 cells in eight sample groups were trypsinized, washed twice by cold PBS and resuspended in 100 μ L $1 \times$ binding buffer at the concentration of 2×10^6 cells/mL. After addition of 5 μ L of Annexin V-FITC, the cells were incubated at room temperature avoiding light for 10 min. Then, 10 μ L of PI was gently mixed in, and incubation continued for 5 min in the same ambient condition. Finally another 400 μ L $1 \times$ binding buffer was added into the flow cytometry tube before cell apoptosis was detected instantly by a FACSCaliber flow cytometer (BD Biosciences, Mountain View, CA, USA). 10,000 cells of each sample were tested. Data analysis was conducted using FlowJo v.10.8.1 software (Tree Star, Inc.).

Animals and Tumor Xenograft Models

All animal experimental procedures were conducted in accordance with the guidance by the Animal Care and Use Committee of Shanghai Jiao Tong University and approved by the Animal Ethics Committee of Shanghai Jiao Tong University (protocol number 202201172). Guidelines for the ethical review of laboratory animal welfare People's Republic of China National Standard GB/T 35892–2018 were followed. To establish the xenograft tumor model, 2×10^6 of ECA 109 cells suspended in 100 μ L of sterile PBS were inoculated subcutaneously into the right flank of each BALB/c-nude mice (5–6 weeks). The mice were used for the next experiments until the tumor size had reached approximately 100 mm³.

In vivo Fluorescent Imaging

The in vivo biodistribution of FRNPs in tumor-bearing nude mice was investigated by in vivo fluorescence imaging. The ECA 109-bearing mice received an intravenous injection with Cy7 labeled FRNPs and the images were captured at indicated time points (0, 1, 6, 12 and 24 h) using a PerkinElmer in vivo imaging system (IVIS spectrum, USA).

MR Imaging

T1-weighted MR imaging was performed on the MAGNETOM Prisma 3.0T. For in vitro imaging, FRNPs at concentrations of 0, 0.00625, 0.0125, 0.025, 0.05, 0.1, 0.2 and 0.4 mM were added to 800 μ L EP tubes for scanning. For in vivo imaging, nude mice bearing ECA 109 tumors were intravenously injected with FRNPs at a manganese concentration of 4 mg/mL (100 μ L). The mice were anesthetized by a peritoneal injection with 7% chloral hydrate and immobilized with adhesive bandage. MR images were scanned using a mouse coil before and after injection.

PA Imaging

After anesthesia induction with isoflurane, tumor-bearing mice with i.v. injection of 100 μ L of FRNPs were placed in a side-lying position and fixed on a mouse handling table equipped with a breathing mask for maintenance anesthesia and ultrasound gel was painted on mice skin of the tumor region. The PA imaging was captured using VEVO LAZR-X multimodal small-animal ultrasound/photoacoustic imaging system (Fujifilm VisualSonics; Toronto; Canada) under the condition with a step size of about 0.076 mm step distance along the long axis of tumors. The maximum contrast PA signal was obtained when the excitation wavelength was 715 nm.

In vivo Synergistic Therapy

Female BALB/c-nude mice were randomly assigned to six groups (n = 5) and received various treatments as follows: (1) PBS; (2) FRNPs alone; (3) FRNPs + NIR; (4) X-ray alone; (5) FRNPs + X-ray; (6) FRNPs + NIR + X-ray. The mice in group 1 received intravenous injection with sterilized PBS solution (100 μ L/mouse). While the mice in group 2, 3, 5 and 6 were administrated with FRNPs solutions (100 μ L, 0.5 mg/mL) through tail vein. 12 h after injection, the mice in group

3 were irradiated with 808 nm NIR laser (150 s, 0.5 W/cm²). Meanwhile, IR images and temperature changes in the tumor region were recorded by an infrared thermal imaging camera before and after laser irradiation. The mice in groups 4, 5 and 6 were exposed to 6 Gy X-ray radiation with a dose rate of 600 MU/min delivered by a varian clinical linear accelerator (6 MeV) using a 10 cm × 10 cm radiation-field and the source-to-skin distance (SSD) was 100 cm. The irradiation treatment was exerted only once for each sample. For group 6, X-ray irradiation was implemented within minutes after 808 nm laser exposure. After the above treatments, Tumor volume and body weight of each mouse were measured every other day until day 14 (n = 5). Digital vernier caliper was employed to measure the tumor volume which were then calculated according to the equation $V = (\text{tumor length}) \times (\text{tumor width})^2 / 2$. On the 14th day, all animals were sacrificed and vital tissues including heart, liver, spleen, lung, kidney, and tumors were harvested and fixed with 4% paraformaldehyde. Hematoxylin and eosin staining and terminal-deoxynucleotidyl transferase mediated dUTP nick end labeling staining were performed for histological diagnosis and analysis of apoptosis.

Statistics

For in vitro and in vivo experiments, tests were carried out at least three times, with results presented in the format of means ± SD unless otherwise specified. Statistical analysis was performed via a two-tailed Student's *t*-test for two groups and one-way ANOVA for various group comparisons using GraphPad Prism 8.0 software (San Diego, CA, USA). P-value < 0.05 was considered to have statistical significance.

Results and Discussion

Preparation and Characterization of FRNPs

In this study, GNCs were firstly prepared according to xia's method, and then, chemotherapy drugs were loaded into the gold nanocages by electrostatic adsorption which were then coated with an ultrathin manganese dioxide (MnO₂) shell, finally, the multifunctional plat 5-FU@GNC@MnO₂ (FRNPs) was successfully prepared. The solutions of GNCs and FRNPs exhibited blue and light brown colors respectively (Figure S1). The morphology of GNCs and FRNPs was examined by transmission electron microscopy (TEM), According to Figure 1A, GNCs presented a hollow spherical

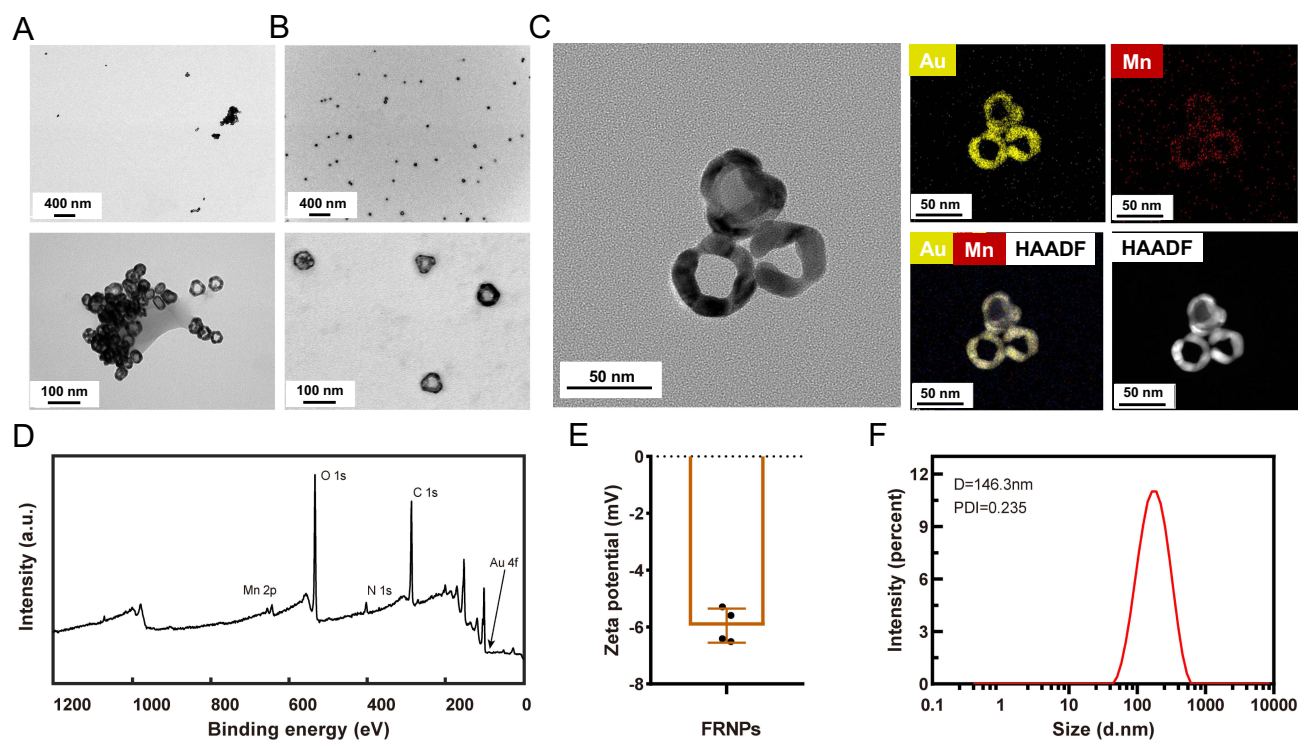


Figure 1 Characterization of FRNPs. (A and B) TEM images of GNCs and FRNPs at different magnifications. (C) The HRTEM and elemental mappings of FRNPs, yellow represents Au and red represents Mn. Scale bar: 50 nm. (D) XPS spectrum of FRNPs. (E) Zeta potential of FRNPs. (F) Dynamic light scattering (DLS) analysis of FRNPs.

shape and showed relatively uniform morphology, which provided the structural basis for drug loading. However, the image also revealed the relatively poor dispersion of bald GNCs. In contrast, a thin cloud layer could be clearly observed around each GNC particle through the TEM image of FRNPs (Figure 1B and S2). It revealed a better morphology and dispersion, and the diameter of FRNPs was around 45 nm. Moreover, FRNPs could be well dispersed in aqueous solution and various physiological buffers (Figure S3 and S4) without showing any apparent aggregation for a relatively long time. To further verify the successful coating of MnO₂ on the surface of GNCs, FRNPs were characterized by HRTEM. From the element mapping images (Figure 1C), it could be clearly seen that Mn element was enriched on the surface of the region where the gold element is located, which proved the existence of MnO₂ outer layer. In addition, X-ray photoelectron spectra (XPS) spectrum of FRNPs in Figure 1D confirmed the presence of Au, Mn, O, C and N elements in FRNPs. The XPS analysis of Au 4f and lattice distance measurement of the cage structure by HRTEM proved the successful preparation of GNCs. Meanwhile, XPS analysis of Mn 2p confirmed the compound states of Mn, proved the successfully surface-modified with MnO₂ on GNCs, imparting the colloidal stability of the FRNPs in aqueous solution for long blood circulation (Figure S5 and S6). The zeta potential of FRNPs was measured to be $\sim -5.95 \pm 0.60$ mV (Figure 1E). Moreover, the average hydrodynamic sizes of FRNPs was $\sim 145.37 \pm 4.47$ nm measured by dynamic light scattering (Figure 1F). Meanwhile, the hydrodynamic sizes of FRNPs at different time points were measured, and the results once again demonstrated that our synthesised FRNPs have excellent dispersion and stability (Figure S7). To verify that 5-FU had been loaded in the GNGs, we measured the UV-Vis spectra of 5-FU, GNC, 5-FU@GNC and 5-FU@GNC@MnO₂ (Figure 2A). Compared with the characteristic absorption peak of 5-FU, FRNPs exhibited the peak of 5-FU at ~ 265 nm, which suggested successful loading of chemotherapeutic drugs. In addition, by analyzing the characteristic absorption peaks of GNGs before and after the coating of MnO₂, it was found that the UV-Vis absorption peak of GNGs was broadened and red-shifted, thus improving the penetration into deep tissues at NIR wavelengths which created better conditions for photothermal therapy and photoacoustic imaging. The red shifting of plasmon band of FRNPs may result from the difference in extinction coefficients between GNGs and MnO₂ shell.

pH-Responsive Drug Release of FRNPs

To simulate the release of 5-FU from the nanoplatform in the weakly acidic tumor microenvironment, drug release test was conducted in PBS buffer at pH 7.4, 6.5 and 5.0 (Figure 2B). Within 2 hours, the cumulative release of 5-FU in pH

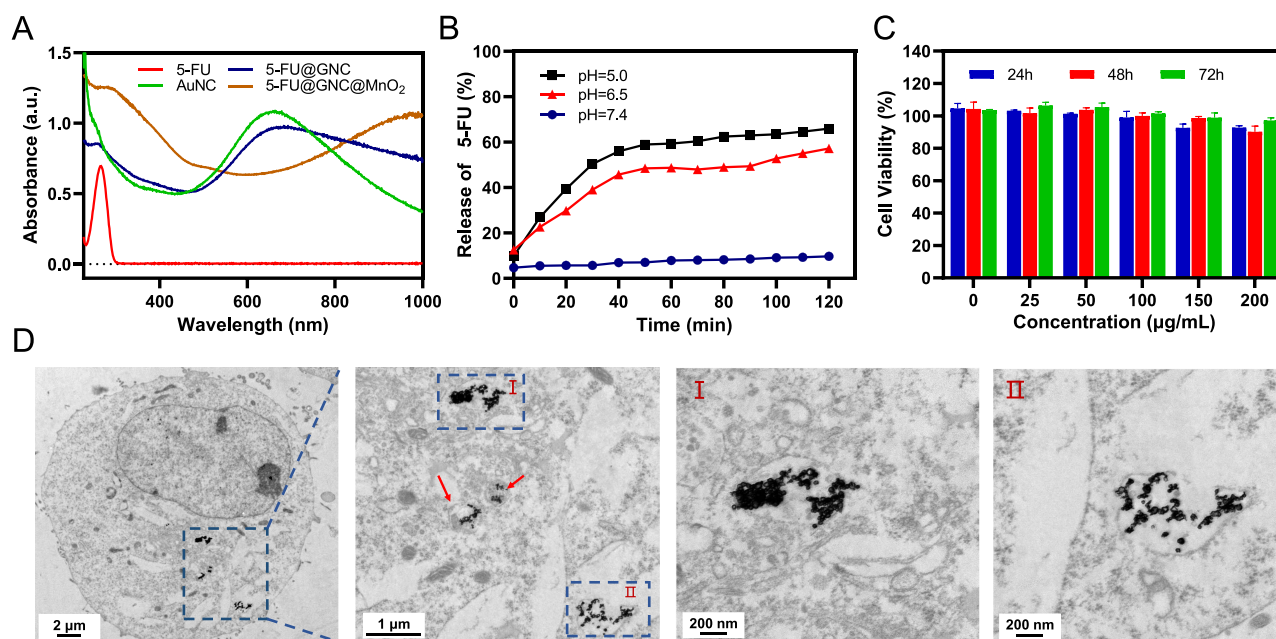


Figure 2 (A) UV-vis absorption spectra of 5-FU, GNC, 5-FU@GNC, and FRNP. (B) In vitro release profiles of 5-FU from FRNPs at pH 7.4, pH 6.5 and pH 5.0. The release profile was determined by recording 5-FU absorbance at 260 nm. (C) Cell viability (CCK-8 assay) for ECA 109 cell line 24, 48, and 72 h after being treated with various concentrations of FRNPs. Data are represented as mean values \pm SD of three replicate samples. (D) TEM images of FRNPs uptake inside ECA 109 cell at different magnifications, blue frames and red arrows identified FRNPs aggregates.

7.4 buffer was less than 10%, which was almost negligible. In contrast, the release of 5-FU in pH 6.5 and 5.0 buffer solution can reach ~60% in a short time. These results indicated that MnO₂ coated on the surface of GNCs could play a good role in blocking chemotherapy drugs inside the cage at the physical pH condition, effectively preventing the early release of drugs in non-tumor sites, thus causing less damage to normal tissues. However, when the FRNPs entered the weakly acidic tumor microenvironment (TME), the surficial MnO₂ was rapidly degraded, and a large number of chemotherapy drugs were released in a short time to play an antitumor role. This mode of drug delivery, in which the loaded drug is released in large quantities in a short period of time, can rapidly increase the drug concentration in the tumour capillaries. Driven by the drug concentration gradient, 5-FU diffuses through the endothelial wall into the surrounding mesenchyme, penetrates deeply and reaches the cancer cells, resulting in greater anti-tumor efficacy.⁵⁸ These results suggested that in the nanoplatform we had built, the drug release performance is pH-responsive, which can not only prevent the early delivery of chemotherapeutic drugs in non-tumor sites, but also realize the expected release of large amounts of drugs in tumor sites, so as to minimize the systemic toxic and side effects of chemotherapeutic drugs.

Cellular Toxicity of FRNPs

CCK-8 assay was performed to evaluate the cytotoxic effect of FRNPs on ECA109 cells. ECA109 cells were cultured with different concentrations of FRNPs ranging from 25 to 200 µg/mL for 24, 48 and 72 h. As shown in [Figure 2C](#), the cell viability showed a slightly concentration-dependent decline, which indicated that the cytotoxic effect of FRNPs increased as concentration increasing. However, no apparent cytotoxicity was observed even at a concentration as high as 200 µg/mL, indicating that FRNPs were highly biocompatible and meets the prerequisite requirements for further biomedical application.

Cellular Uptake and Distribution of FRNPs

To a great extent, the antitumor effects of nanoparticles is largely determined by the amount of therapeutic agent internalized by tumor cells. In this study, the cellular uptake and localization of FRNPs in ECA109 cells was investigated by biological TEM. ECA109 cells were incubated with FRNPs for 24 h, and then imaged by biological TEM for further analysis. Since Au has a high electronic density, FRNPs appeared as high contrast in the TEM image, which was easy to detect and distinguish from the cellular structure. The bio-TEM results ([Figure 2D](#)) showed that there were a large number of FRNPs accumulated in the cytoplasm, most of them were internalized as clusters and trapped in vesicles, either endosomes or lysosomes, and few clusters were released from the lysosomes and entered the cytosols. Most nanomaterials are degraded by lysosomes after entering the cell through endocytosis. However, due to their unique metal properties, gold nanoparticles can usually escape from lysosomes and enter the cytoplasm. To quantify the cellular uptake of FRNPs, flow cytometry was employed to detect the fluorescence of Cy7-FRNPs in ECA109 cells. The mean fluorescence intensity (MFI) of Cy7-FRNPs-treated cells is 2.5-fold higher than that of the untreated control group after 24 h incubation ([Figure S8](#)). The rapid and effective uptake of FRNPs by ECA109 cells laid a solid foundation for the follow-up in vitro and in vivo experiments of therapeutic efficacy verification.

Photothermal Effect

Motivated by the broad absorption spectra located in the NIR region, the potential of FRNPs as a PTT agent was explored. First, we verified the photothermal effect of FRNPs solution with various concentrations. As depicted in the thermal images ([Figure 3A](#)) and corresponding curves for temperature changes ([Figure 3B](#)), the temperature of sterile PBS maintained at ~20 °C, showing negligible temperature change under 808 laser irradiation (1.5 W/cm²). In contrast, under the same experimental conditions, the temperature of FRNPs solution with different concentrations increased rapidly within just 100 s, and then reached the platform level. The heating rate and the maximum temperature were positively correlated with the concentration of the suspended nanoplatform solution. The higher the concentration, the faster the heating rate rises and the higher the final temperature reaches. The temperature of FRNPs with the highest concentration (100 µg/mL) could reach about 60 °C after 180 s of laser irradiation, and the suspension quickly cooled down below physiological temperature (37 °C) within 50s when the laser was turned off ([Figure 3C](#)). The above results indicated that FRNPs could rapidly convert light energy into heat with high efficiency, which may cause irreversible cell damage owing to hyperthermia. Since poor photostability would greatly limit the therapeutic effect of photothermal agents, we performed six cycles of 808 nm laser on/off experiments to further evaluate the photothermal stability of FRNPs. 100 µg/mL FRNPs solution was exposed to NIR laser radiation for 3 min, and then the laser was immediately turned off to

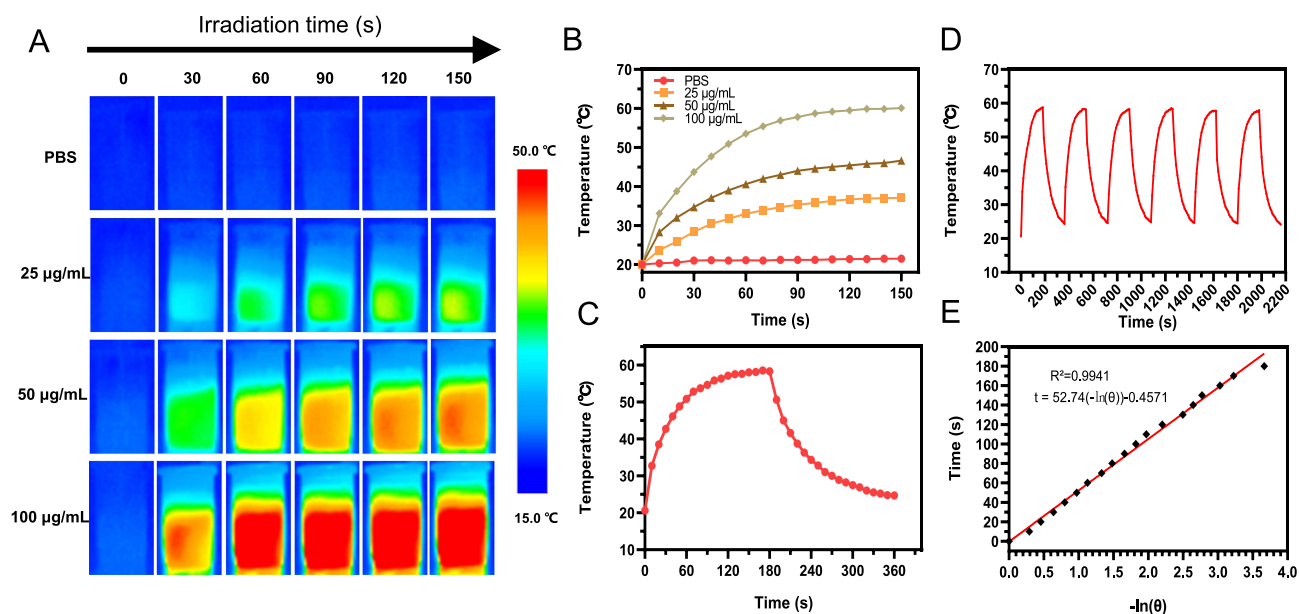


Figure 3 Photothermal performance of FRNPs. (A) Representative thermal images of FRNPs dispersion in PBS (0–100 µg/mL) during laser irradiation with an 808 nm laser at 1.5 W/cm². (B) Photothermal conversion properties of FRNPs at different concentrations under 808 nm laser irradiation with the power density of 1.5 W/cm². PBS was used as the negative control group. (C) Heating and cooling curves of FRNPs aqueous suspension under 808 nm laser irradiation at a power density of 1.5 W/cm². (D) Temperature changes of FRNPs (100 µg/mL) over six laser on/off cycles upon 808 laser irradiation. (E) Linear time data versus $-\ln(\theta)$ obtained from the cooling period.

let the FRNPs solution experience a natural cooling for another 3 min. Afterwards the above process was repeated. As shown in Figure 3D, the temperature trend of each cycle is relatively consistent with each other and no obvious dropping was detected during the temperature elevation, which suggested that FRNPs owned a favorable photothermal stability. According to the fitting curve (Figure 3E), the photothermal conversion efficiency (η) of FRNPs was calculated to be 32.25%. All these results revealed that our synthesized FRNPs may be an excellent candidate as a kind of photothermal agent in cancer treatment.

In vitro Synergistic Therapy

Considering that Au as high-Z element has a strong photoelectric effect, we further evaluated the radiosensitization ability of FRNPs. Meanwhile the anti-tumor effect of FRNPs on ECA 109 cells in combination therapy was investigated in view of the promising biocompatibility and excellent photothermal performance of FRNPs. The colony formation assay was conducted to assess the self-renewal capacity of ECA 109 cells under different treatments based on the ability of individual cells to grow into colonies. The colony formation pictures of eight various treatment groups were shown in the Figure 4A. It could be clearly seen that the number of colonies in FRNPs and FRNPs + NIR groups significantly decreases under X-ray irradiation compared with that in X-ray only group, which suggested that the presence of FRNPs may increase the proliferation injury and verified the radiosensitizing power of FRNPs. The survival fraction of cells under gradient doses of radiation was explored. As the survival fraction curve shows, obvious radiosensitization effect could be observed with the increase of radiation dose in FRNPs and FRNPs + NIR groups, while the NIR alone group has almost no enhancement effect compared with control group (Figure 4B). The sensitization enhancement ratio (SER) which reflects the ability of different treatments to enhance the radiotherapy was obtained using the classical multitarget single-hit model. The SER was calculated to be 1.17, 1.33 and 1.76 respectively, which corresponded to NIR, FRNPs, and FRNPs + NIR groups (Figure 4C). It is worth noting that only when FRNPs were added, the radiosensitization rate is 1.33, while when combined with NIR, the radiosensitization rate increased to 1.76. The results not only proved that FRNPs owned excellent radiosensitization efficiency, but also showed the superiority of combined treatment to single treatment, as the SER of the synergistic treatment group was much higher than that of the single treatment group. In order to evaluate the effect of radiosensitization more intuitively, confocal microscopy was employed to analyze the DNA double-strand breaks of each group. In the immunofluorescence images, nuclei were stained as blue by DAPI, and DNA double-strand breaks were labeled by Alexa fluor 488 appearing as green fluorescent spots. It can be seen from the Figure 4D that there was only a few

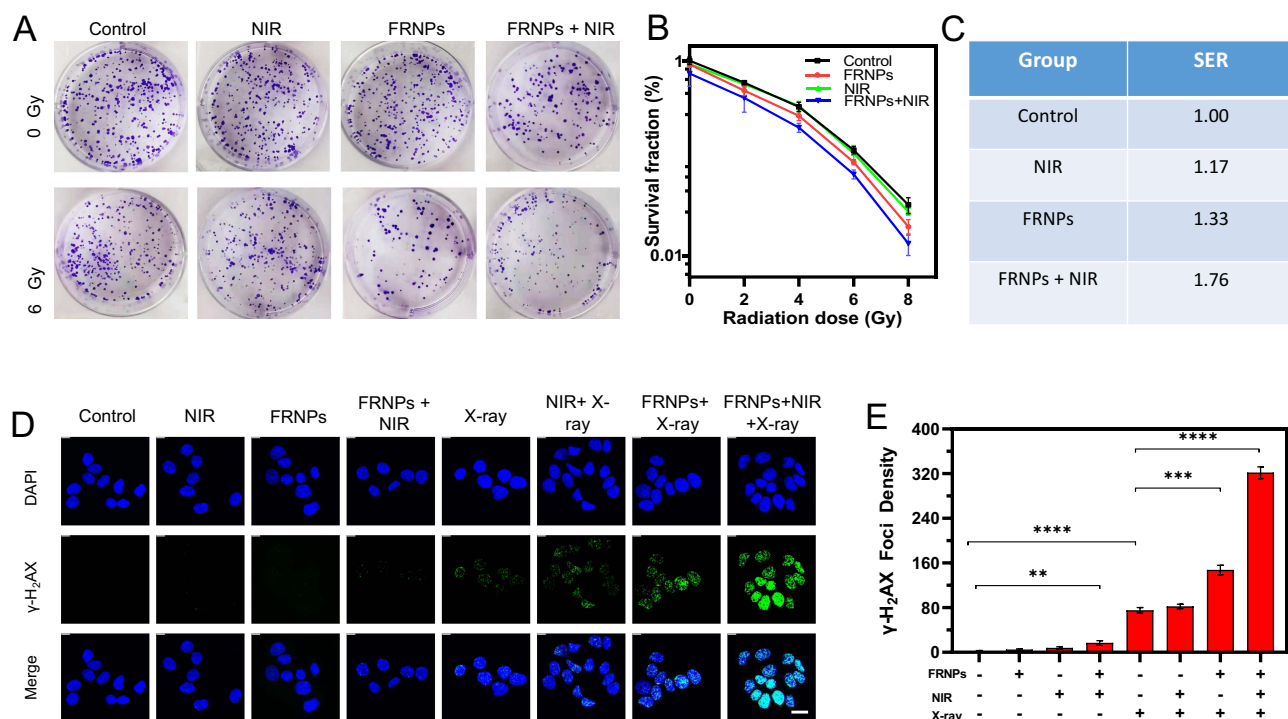


Figure 4 Sensitization effect study of FRNPs on ECA 109 cells. (A) Colony formation images of ECA 109 cells treated with FRNPs (100 μ g/mL) and/or laser irradiation and/or X-ray radiation (6 Gy). (B) Surviving fractions of ECA 109 cells treated with or without FRNPs and/or laser irradiation at radiation doses of 0, 2, 4, 6, and 8 Gy. Data represent as mean \pm SD of at least three identically and independently prepared samples. (C) Sensitization enhancement ratio (SER) of control, NIR, FRNPs, and FRNPs + NIR calculated by the multitarget single-hit model. (D) The representative images of ECA 109 cells in different treatment groups stained with γ -H₂AX. DAPI was used as a nuclear marker (scale bar = 10 nm). (E) Normalized γ -H₂AX fluorescent spots number of different groups (n = 3). P values were calculated by the Student's test: **p < 0.01, ***p < 0.001, ****p < 0.0001.

amount of γ -H₂AX foci (green fluorescent spots) in the nuclei of cells without X-ray irradiation, no matter the FRNPs were added or not. In contrast, a relatively high level of γ -H₂AX foci were clearly observed within the nuclei of cells exposed to X-ray. Furthermore, in the FRNPs + NIR + X-ray group, the number of γ -H₂AX foci significantly increased, showing as dense and bright green fluorescence in the nuclei, indicating that in the presence of FRNPs and NIR, the radiation had a strong damage effect on DNA. Next, we quantified the DNA double-strand breaks. The normalized amount of γ -H₂AX in each cell were obtained by dividing the total number of cells in one field by the number of green fluorescent dots in the field. In the X-ray irradiation groups, an obvious elevation in the number of γ -H₂AX per cell was observed and there was a statistically significant difference between cells in the presence and absence of FRNPs. This confirmed the radiosensitization ability of FRNPs in radiotherapy. Moreover, the number of γ -H₂AX per cell was the largest in the cells treated with FRNPs + NIR + X-ray, which was 4.3-fold compared to cells in the X-ray only group (Figure 4E).

In order to observe the cell survival fraction of different treatment groups more intuitively, we quantified the results obtained from colony formation assay. The survival fraction of the cells treated with FRNPs alone is 97%. However, the cell survival fraction decreased to 84% after NIR photothermal treatment, while the percentage declines to 50% after X-ray radiations, much lower than NIR or X-ray radiation treatment alone without FRNPs, which indicated that FRNPs are both excellent photothermal agents and radiosensitizers. Furthermore, the combined effect of FRNPs-mediated photothermal and X-ray radiation treatment was also explored. The results revealed that the cell survival fraction drastically dropped to 33% after dual treatment, which presented 51% and 27% below FRNPs-mediated PTT and RT (Figure S9). The results demonstrated that FRNPs-mediated photothermal therapy could enhance the FRNPs-mediated radiotherapy to the utmost extent.

In order to further evaluate the therapeutic efficacy of different treatments, calcein-AM/PI dual staining were carried out. As shown in the fluorescence images (Figure 5A), red represents dead cells and green represents living cells. It can be seen from the results that there were only a few dead cells in the Control, NIR only, FRNPs only, X-ray only and NIR + X-ray groups. In the FRNPs + NIR and FRNPs + X-ray group, the number of dead cells began to increase, indicating that FRNPs are excellent PTT agents and radiosensitizer. In the FRNPs + NIR + X-ray group, only sporadic living cells

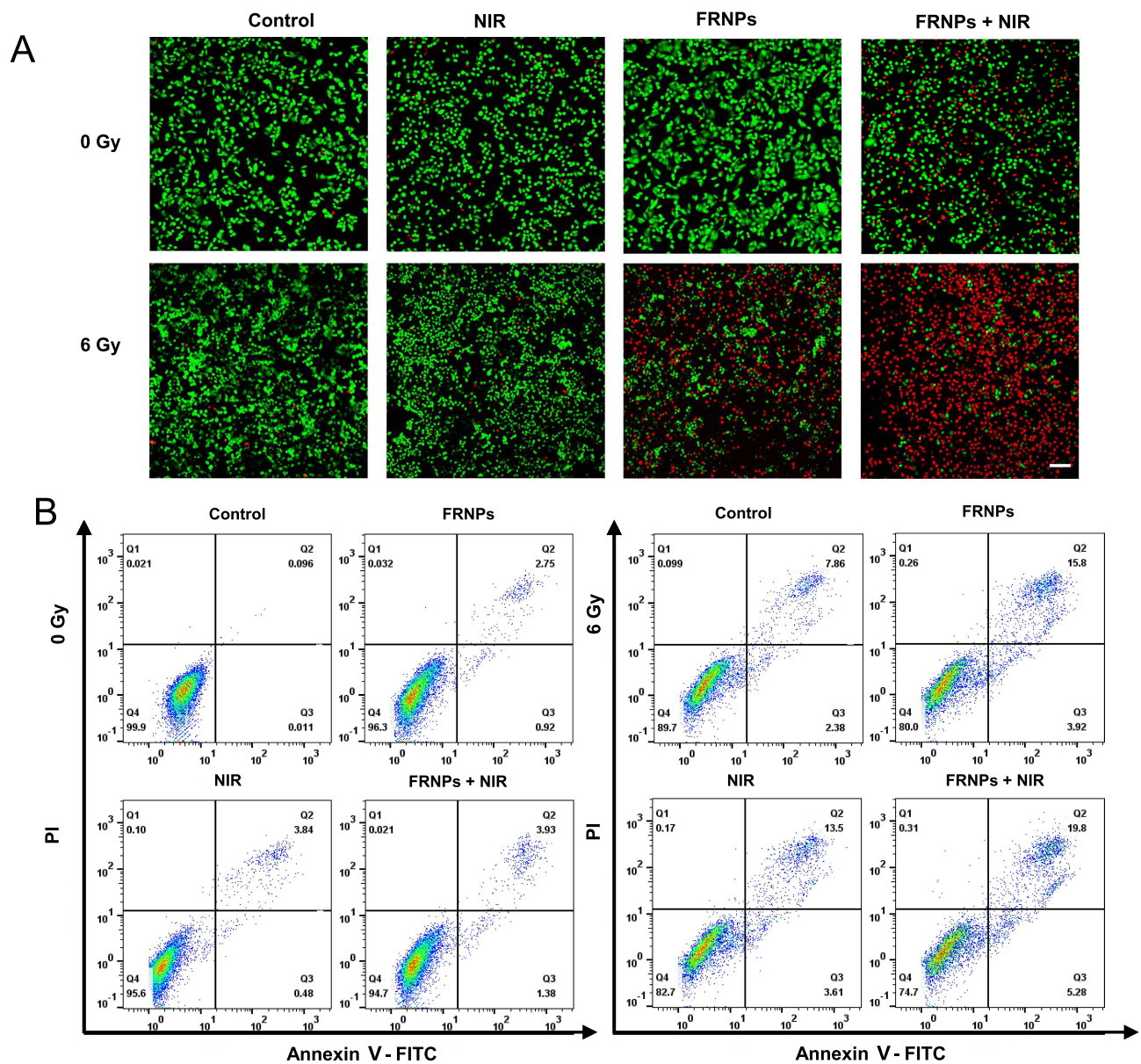


Figure 5 Therapeutic efficacy of FRNPs in vitro. **(A)** Live/dead staining of ECA 109 cells with various treatments (scale bar is 100 μ m). **(B)** Apoptosis and necrosis of ECA 109 cells with various treatments analyzed by flow cytometry.

were found in a large number of dead cells, which revealed that the combined therapy had strong anti-tumor efficacy and was significantly superior to other treatment groups.

At the same time, flow cytometry assay was performed using Annexin V-FITC/PI apoptosis detection kit to investigate the ratio of apoptosis and necrosis induced by different treatments. As shown in the [Figure 5B](#) and [S10](#), the treatment groups showed varying degrees of cell apoptosis and/or necrosis compared to the control group. In the experimental groups without X-ray irradiation, the proportion of cell apoptosis and/or necrosis caused by FRNPs-mediated photothermal therapy was the highest. In the four groups treated with X-ray, the cell apoptosis ratio showed a significant increase after the addition of FRNPs. The highest total apoptosis rate was 25.08% in the FRNPs + NIR + X-ray comprehensive treatment group, and the proportion of early and late apoptosis was 5.28% and 19.8% respectively. The results of apoptosis experiment were consistent with those of colony experiment and live/death cell staining experiment. It was once again proved that the combination of FRNPs-mediated photothermal therapy, radiotherapy and chemotherapy could kill tumor cells in the maximum extent, verifying the advantage of complex therapy.

In vivo Biodistribution Studies and Multimodal Imaging of FRNPs

Mastering the distribution of nanoparticles at tumor sites over time is crucial for selection of treatment time point. To study the distribution and tumor-targeting ability of FRNPs in vivo, fluorescence imaging was carried out in tumor bearing nude mice. FRNPs were labelled with a NIR sensitive dye Cy7 to realize the tracing of nanoparticles in mice. Cy7-FRNPs were first injected into mice through the tail vein, after which NIR fluorescence imaging was performed at specific time points. The results (Figure 6A) showed that FRNPs were transported to the whole body with blood circulation, and fluorescence intensity at different parts changed with time. Due to the first pass effect, fluorescent signal first appeared in the liver. At the tumor site, fluorescence signal began to appear at 6 h after injection, and then the signal intensity gradually increased, reaching the maximum at 12 h (Figure 6A and S11). With the prolongation after the injection, the fluorescence signal of the liver gradually weakened and almost disappeared at 24 h after injection. However, the signal of the tumor site was still strong which indicated that FRNPs have excellent tumor passive targeting and retention ability. The long retention of FRNPs at the tumor region may be related to the appropriate size. For MR imaging, we first performed MR scanning for FRNPs with gradient concentrations, and found a concentration-dependent brightening effect in T1-weighted images (Figure 6B). Subsequently, we verified the imaging ability of FRNPs in tumor-bearing mice. MR Images before and after intravenous FRNPs injection were compared, and remarkable enhancement of T1-weighted signal was observed at tumor site (Figure 6C). According to the Figure 6D, the T1 relaxation rate of FRNPs was calculated to be $4.76 \text{ mM}^{-1} \text{ S}^{-1}$, which is comparable or even superior to other T1 contrast agent used in clinic or biomedicine (Table S1), suggesting that our FRNPs possessed great magnetic resonance imaging capability. At the same time, due to the high density and extinction coefficients of FRNPs, photoacoustic imaging was also conducted. As shown in the Figure 6E and S12, a significantly enhanced photoacoustic signals appeared in the tumor region upon 12 h after FRNPs administration. All the above results not only show that FRNPs can effectively passively aggregate at the tumor site through EPR effect, but also can be used as efficient contrast agents for MR and PA imaging to achieve multimodal image-guided comprehensive therapy.

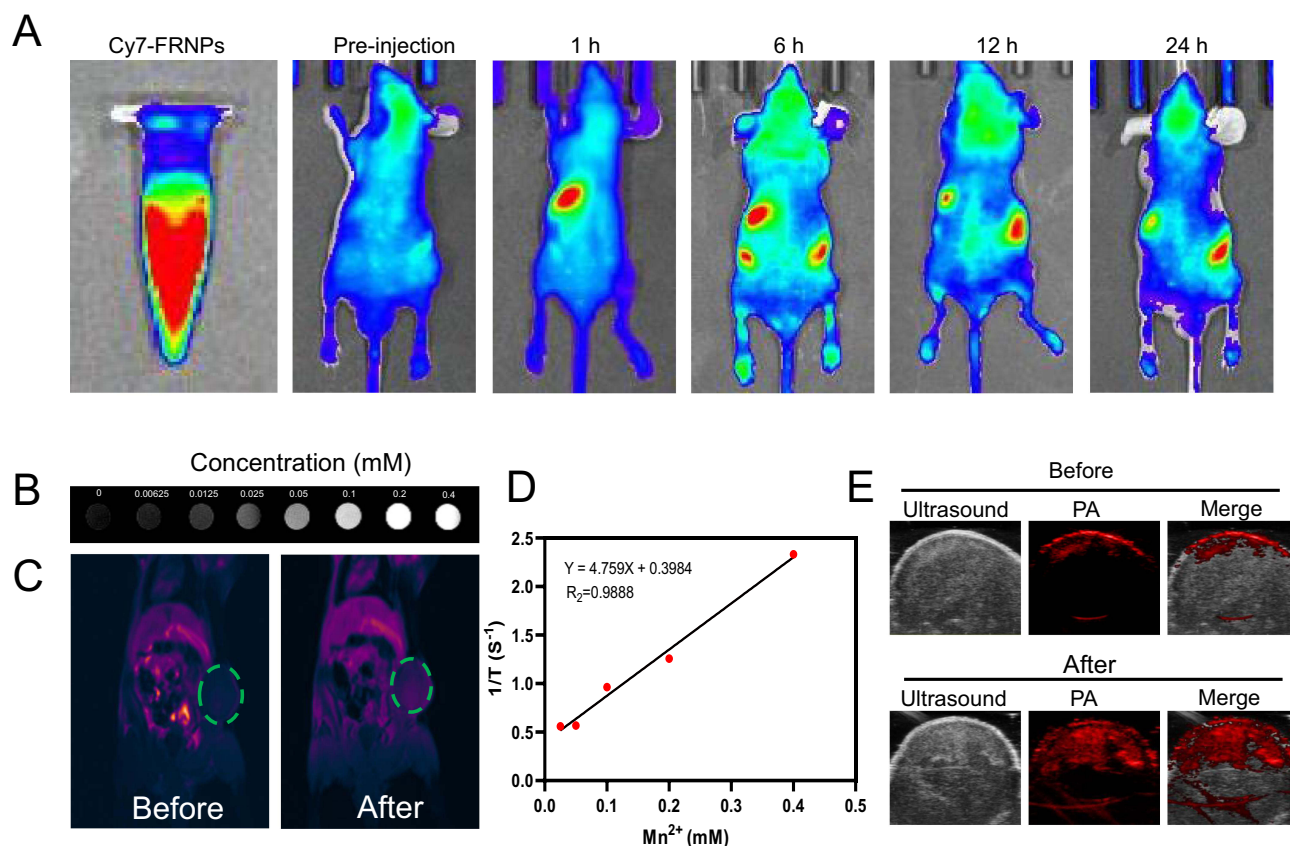


Figure 6 In vivo biodistribution studies and multimodal imaging of FRNPs. (A) In vitro fluorescence imaging of Cy7-FRNPs and in vivo fluorescence imaging of ECA 109 tumor-bearing mice after the treatment of Cy7-FRNPs for pre-injection, 1, 6, 12, and 24 h. (B) T1-weighted MR images of FRNPs solutions at various concentrations. (C) In vivo MR images of mice before and after i.v. injection with FRNPs, green circled area identified tumor site. (D) T1 relaxation rates (R1) of FRNPs solutions at different Mn concentrations. (E) In vivo PA images of mice before and after i.v. injection with FRNPs.

In vivo Therapeutic Performance

Encouraged by the experimental results of the effective killing of tumor cells by the nanoprobe in vitro, we further studied the therapeutic efficacy of FRNPs in vivo. The schematic of detailed treatment procedure was shown in Figure 7A. First, we used near-infrared thermal imaging to real-time monitor the temperature changes at the tumor site of tumor bearing mice after different treatments. During the 150 s period of 808 nm near-infrared laser irradiation, the temperature changes at the tumor region of each group of tumor bearing mice are shown in Figure 7B, the tumor

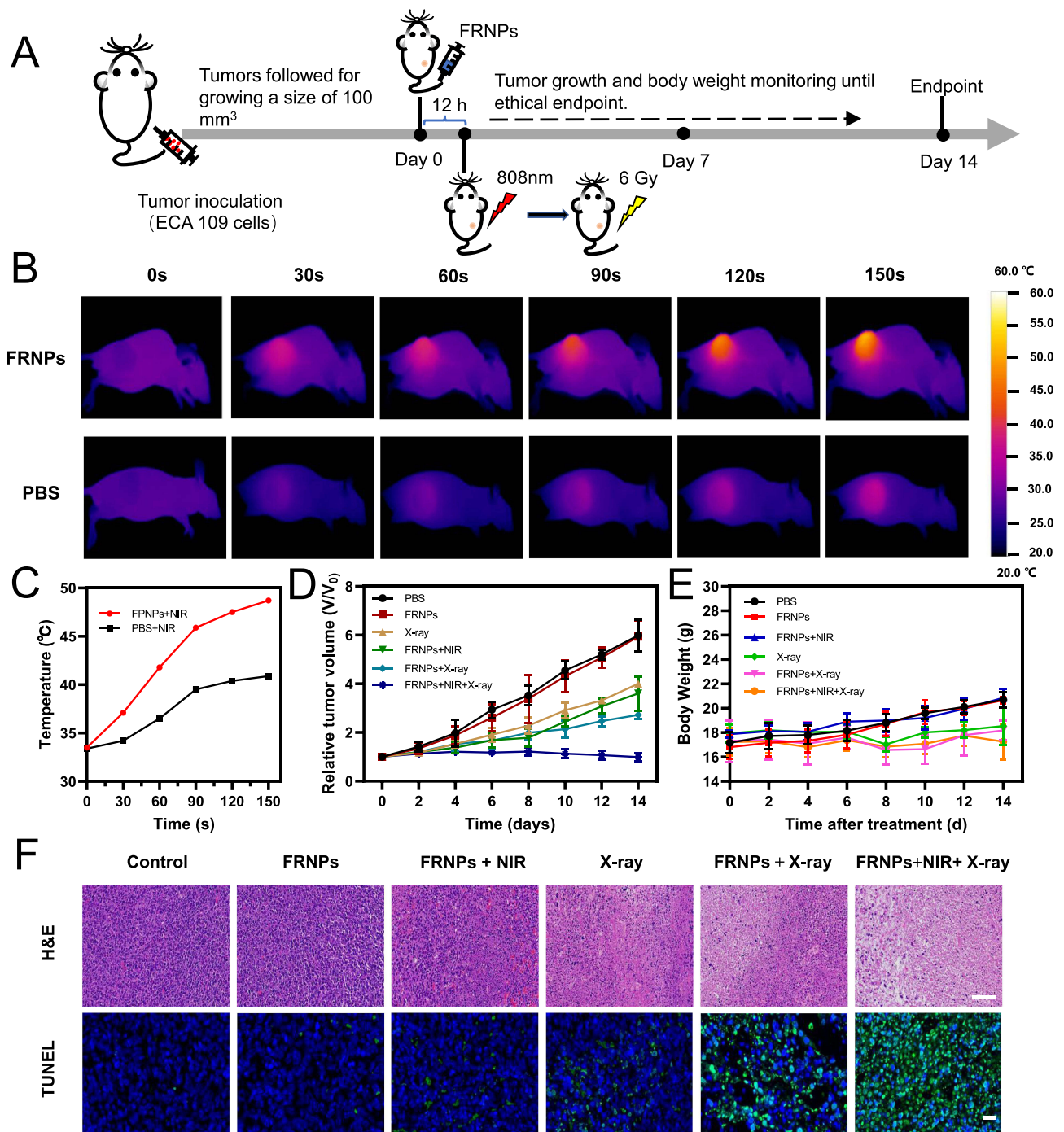


Figure 7 Therapeutic efficacy of FRNPs in vivo. (A) Schematic illustration of the in vivo treatment schedule. (B) Representative infrared thermal images of tumor-bearing mice injected with PBS or 100 μL 0.5 mg/mL FRNPs during laser irradiation. 808 nm laser was applied 12 h after injection FRNPs at a power density of 0.5 W/cm² for 150 s. (C) The temperature change curves of tumors during 150 s laser irradiation. (D) Relative tumor volume growth curves of mice after various treatments. (E) Body weight of mice in each treatment group (n=5). (F) H&E (scale bar = 100 μm) and TUNEL (scale bar = 20 μm) stained tumor images of different groups at the 14th day after various treatments.

surface temperature increased from 33.5 °C to 48.7 °C in just 150 s, while the control group had only a slight temperature change (Figure 7C). This further proves the potential of FRNPs as photothermal agents for tumor thermal ablation *in vivo*.

Secondly, the tumor-bearing mice in each group received different treatments. The tumor volume changes of tumor-bearing mice in each treatment group were shown in Figure 7D, the PBS group and the FRNPs alone group showed similar tumor growth characteristics during the efficacy observation period, indicating that the antitumor effect of FRNPs alone is very limited. FRNPs-mediated photothermal therapy or radiotherapy could restrict tumor proliferation to a certain extent. Moreover, the FRNPs-mediated radiotherapy group showed a more effective tumor growth delay compared with the X-ray only group, which revealed that FRNPs also owned an excellent radiosensitization ability *in vivo*. In the combined treatment group mediated by FRNPs, tumor growth was almost completely inhibited, showing the most efficient tumor growth suppression. The reason may be that FRNPs-mediated hyperthermia and the enzyme activity of MnO₂ create an oxygen-rich environment, reducing the RT resistance of hypoxic cells. In addition, the loaded 5-FU not only had cytotoxicity but also had a certain radiosensitizing effect, thus maximizing the anti-tumor efficiency of X-ray. No significant weight change was observed in all treatment groups suggesting that all the treatment regimens were tolerated and safe in animals (Figure 7E). To further validate the antitumor efficacy of various treatments at tissue level and cell level, subcutaneous tumor was harvested from mice at the end of the treatment and subjected to H&E and TUNEL staining. The staining results showed that compared with other treatment groups, tumor tissues in the combined treatment group exhibited the most extensive structural destruction and cell necrosis (Figure 7F).

Finally, the *in vivo* biocompatibility of FRNPs was analyzed by H&E staining of major organs. As shown in Figure 8, compared with the control group, no obvious organ damage and abnormal pathological changes, such as inflammation or hyperplasia, were observed in all the experimental groups, which indicated that FRNPs had no obvious toxic side effects *in vivo*. In summary, the above experimental results demonstrate that our synthesized FRNPs can effectively mediate the synergistic treatment of photothermal therapy combined with radiotherapy under the premise of ensuring biosafety, thus playing a powerful role in killing tumor *in vivo*.

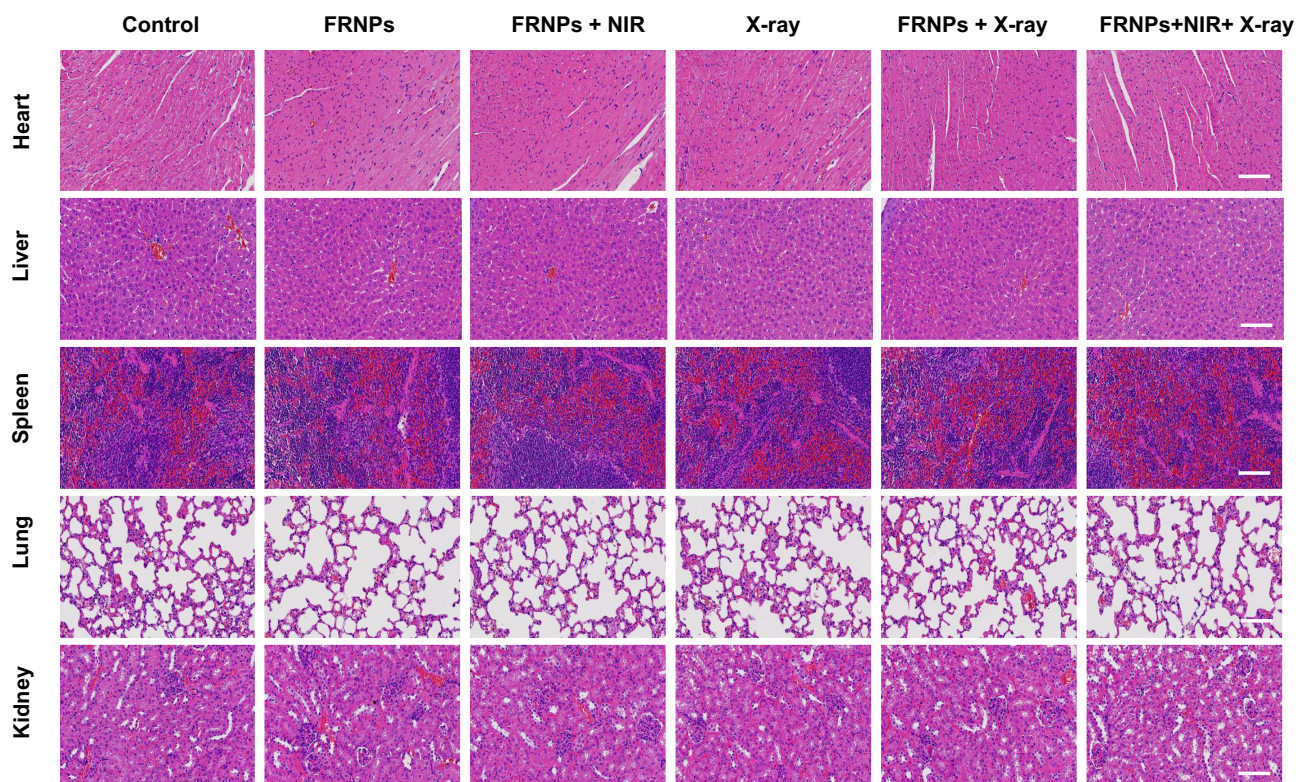


Figure 8 Representative images of H&E staining for main organs of each treatment group (scale bar = 100 μm).

Conclusion

In conclusion, a nanoscale multifunctional theranostic system based on FRNPs through the integration of GNCs with MnO₂ has been fabricated for MR-PA multimodal imaging and PTT/RT/CT synergistic cancer treatment. The synthetic FRNPs have good biocompatibility, with no obvious toxicity in both in vitro and in vivo experiments. Moreover, FRNPs were proved to be effective photothermal conversion agent and radiosensitizer whose photothermal conversion efficiency (η) and sensitization enhancement ratio (SER) was 32.25% and 1.33 respectively. When FRNPs accumulate in tumor tissue, the tumor was first ablated by photothermal therapy and simultaneously became more sensitive to radiation therapy. Then under X-ray irradiation, FRNPs significantly sensitized tumor cells to radiation. At the same time, MnO₂ on the surface of GNCs degraded in the acidic tumor microenvironment. This degradation causes the rapid release of 5-FU within the GNCs, further improving the therapeutic effect due to the synergistic effect, thus causing more cancer cell deaths. In vivo treatment studies further confirmed that FRNPs-mediated comprehensive therapy led to the most effective tumor growth inhibition and tumor destruction. In terms of imaging, FRNPs exhibited an excellent T1-weighted MR and PA imaging potential at tumor site, which could passively gather at the tumor site via EPR effect, precisely delineating the tumor location in vivo. Taken together, FRNPs can effectively inhibit the growth of esophageal cancer through programmed photothermal therapy, radiotherapy and chemotherapy at low radiotherapy doses. The current combination therapy strategy provides a novel idea to break the barrier of traditional radiotherapy.

Acknowledgments

This work was financially supported by the National Natural Science Foundation of China (Grant No. 82073380, 81971714 and 8202010801), the Interdisciplinary Program of Shanghai Jiao Tong University (YG2022ZD011 and YG2021QN130) and the China Postdoctoral Science Foundation (No. 2020TQ0191).

Disclosure

The authors report no conflicts of interest in this work.

References

1. Sung H, Ferlay J, Siegel RL, et al. Global cancer statistics 2020: GLOBOCAN estimates of incidence and mortality worldwide for 36 cancers in 185 countries. *CA Cancer J Clin.* 2021;71(3):209–249. doi:10.3322/caac.21660
2. Smyth EC, Lagergren J, Fitzgerald RC, et al. Oesophageal cancer. *Nat Rev Dis Primers.* 2017;3:17048. doi:10.1038/nrdp.2017.48
3. Luan SY, Xie R, Yang YS, et al. Acid-responsive aggregated gold nanoparticles for radiosensitization and synergistic chemoradiotherapy in the treatment of esophageal cancer. *Small.* 2022;18(19). doi:10.1002/sml.202200115
4. Xie J, Gong L, Zhu S, Yong Y, Gu Z, Zhao Y. Emerging strategies of nanomaterial-mediated tumor radiosensitization. *Adv Mater.* 2019;31(3):e1802244. doi:10.1002/adma.201802244
5. Yang S, Han GH, Chen Q, et al. Au-Pt nanoparticle formulation as a radiosensitizer for radiotherapy with dual effects. *Int J Nanomed.* 2021;16:239–248. doi:10.2147/IJN.S287523
6. Hu P, Hou X, Yu XJ, et al. Folic acid-conjugated gold nanostars for computed tomography imaging and photothermal/radiation combined therapy. *ACS Appl Bio Mater.* 2021;4(6):4862–4871. doi:10.1021/acsbm.1c00171
7. Liu Q, Shi Y, Chong Y, Ge CC. Pharmacological ascorbate promotes the tumor radiosensitization of Au@Pd nanoparticles with simultaneous protection of normal tissues. *ACS Appl Bio Mater.* 2021;4(2):1843–1851. doi:10.1021/acsbm.0c01537
8. Liu X, Zhang X, Zhu M, et al. PEGylated Au@Pt nanodendrites as novel theranostic agents for computed tomography imaging and photothermal/radiation synergistic therapy. *ACS Appl Mater Inter.* 2017;9(1):279–285. doi:10.1021/acsbm.6b15183
9. Du Y, Sun H, Lux F, et al. Radiosensitization effect of AGuIX, a gadolinium-based nanoparticle, in non-small cell lung cancer. *ACS Appl Mater Inter.* 2020;12(51):56874–56885. doi:10.1021/acsbm.0c16548
10. Wang X, Zhang CY, Du JF, et al. Enhanced generation of non-oxygen dependent free radicals by schottky-type heterostructures of Au-Bi₂S₃ nanoparticles via X-ray-induced catalytic reaction for radiosensitization. *Acs Nano.* 2019;13(5):5947–5958. doi:10.1021/acsnano.9b01818
11. Liu R, Zhang X, Zhang Q, et al. Adjuvant radiotherapy of involved field versus elective lymph node in patients with operable esophageal squamous cell cancer: a single institution prospective randomized controlled study. *J Cancer.* 2021;12(11):3180–3189. doi:10.7150/jca.50108
12. Yang LT, Zhou L, Chen L, Liang SX, Huang JQ, Zhu XD. Establishment and verification of a prediction model for symptomatic radiation pneumonitis in patients with esophageal cancer receiving radiotherapy. *Med Sci Monit.* 2021;27:e930515.
13. Alhussan A, Bozdogan EPD, Chithrani DB. Combining gold nanoparticles with other radiosensitizing agents for unlocking the full potential of cancer radiotherapy. *Pharmaceutics.* 2021;13(4):442. doi:10.3390/pharmaceutics13040442
14. Ma NN, Jiang YW, Zhang XD, et al. Enhanced radiosensitization of gold nanospikes via hyperthermia in combined cancer radiation and photothermal therapy. *ACS Appl Mater Inter.* 2016;8(42):28480–28494. doi:10.1021/acsbm.6b10132
15. Kuang Y, Zhang Y, Zhao Y, et al. Dual-stimuli-responsive multifunctional Gd(2)Hf(2)O(7) nanoparticles for MRI-guided combined chemo-/photothermal-/radiotherapy of resistant tumors. *ACS Appl Mater Inter.* 2020;12(32):35928–35939. doi:10.1021/acsbm.0c09422

16. Rajani C, Patel V, Borisa P, et al. Photothermal therapy as emerging combinatorial therapeutic approach. *Future Pharma Prod Develop Res.* 2020;2020:297–339.
17. Dou Y, Yang X, Yang WT, et al. PB@Au core-satellite multifunctional nanotheranostics for magnetic resonance and computed tomography imaging in vivo and synergetic photothermal and radiosensitive therapy. *ACS Appl Mater Inter.* 2017;9(2):1263–1272. doi:10.1021/acsami.6b13493
18. Wang J, Tan X, Pang X, Liu L, Tan F, Li N. MoS₂ quantum Dot@polyaniline inorganic-organic nanohybrids for in vivo dual-modal imaging guided synergistic photothermal/radiation therapy. *ACS Appl Mater Inter.* 2016;8(37):24331–24338. doi:10.1021/acsami.6b08391
19. Yin M, Chen X, Guo Q, et al. Ultrasmall zirconium carbide nanodots for synergistic photothermal-radiotherapy of glioma. *Nanoscale.* 2022;14(40):14935–14949. doi:10.1039/D2NR04239H
20. Zhang C, Men D, Zhang T, et al. Nanoplatfoms with remarkably enhanced absorption in the second biological window for effective tumor thermoradiotherapy. *ACS Appl Mater Inter.* 2020;12(2):2152–2161. doi:10.1021/acsami.9b20677
21. Bao J, Zu X, Wang X, et al. Multifunctional Hf/Mn-TCPP Metal-organic framework nanoparticles for triple-modality imaging-guided PTT/RT synergistic cancer therapy. *Int J Nanomed.* 2020;15:7687–7702. doi:10.2147/IJN.S267321
22. Li E, Cheng X, Deng Y, et al. Fabrication of PEGylated Fe@Bi(2)S(3) nanocomposites for dual-mode imaging and synergistic thermoradiotherapy. *Biomater Sci.* 2018;6(7):1892–1898. doi:10.1039/C8BM00336J
23. Li Y, Sun Y, Cao T, et al. A cation-exchange controlled core-shell MnS@Bi(2)S(3) theranostic platform for multimodal imaging guided radiation therapy with hyperthermia boost. *Nanoscale.* 2017;9(38):14364–14375. doi:10.1039/C7NR02384G
24. Li A, Li X, Yu X, et al. Synergistic thermoradiotherapy based on PEGylated Cu(3)BiS(3) ternary semiconductor nanorods with strong absorption in the second near-infrared window. *Biomaterials.* 2017;112:164–175. doi:10.1016/j.biomaterials.2016.10.024
25. Cheng L, Shen S, Shi S, et al. FeSe(2)-Decorated Bi(2)Se(3) nanosheets fabricated via cation exchange for chelator-free (64)Cu-labeling and multimodal image-guided photothermal-radiation therapy. *Adv Funct Mater.* 2016;26(13):2185–2197. doi:10.1002/adfm.201504810
26. Frantellizzi V, Verrina V, Raso C, et al. 99mTc-labeled keratin gold-nanoparticles in a nephron-like microfluidic chip for photo-thermal therapy applications. *Mat Today Adv.* 2022;16:100286. doi:10.1016/j.mtadv.2022.100286
27. Lee SB, Ahn SB, Lee S-W, et al. Radionuclide-embedded gold nanoparticles for enhanced dendritic cell-based cancer immunotherapy, sensitive and quantitative tracking of dendritic cells with PET and Cerenkov luminescence. *NPG Asia Materials.* 2016;8(6):e281–e281. doi:10.1038/am.2016.80
28. Daems N, Michiels C, Lucas S, Baatout S, Aerts A. Gold nanoparticles meet medical radionuclides. *Nucl Med Biol.* 2021;100–101:61–90. doi:10.1016/j.nucmedbio.2021.06.001
29. Yoshida A, Kitayama Y, Hayakawa N, et al. Biocompatible polymer-modified gold nanocomposites of different shapes as radiation sensitizers. *Biomater Sci.* 2022;10(10):2665–2672. doi:10.1039/D2BM00174H
30. Yang ZB, Huang S, Liu Y, et al. Biotin-Targeted Au(I) radiosensitizer for cancer synergistic therapy by intervening with redox homeostasis and inducing ferroptosis. *J Med Chem.* 2022;65(12):8401–8415. doi:10.1021/acs.jmedchem.2c00300
31. Tudda A, Donzelli E, Nicolini G, et al. Breast radiotherapy with kilovoltage photons and gold nanoparticles as radiosensitizer: an in vitro study. *Med Phys.* 2022;49(1):568–578. doi:10.1002/mp.15348
32. Piccolo O, Lincoln JD, Melong N, et al. Radiation dose enhancement using gold nanoparticles with a diamond linear accelerator target: a multiple cell type analysis. *Sci Rep.* 2022;12(1). doi:10.1038/s41598-022-05339-z
33. Marques A, Belchior A, Silva F, et al. Dose rate effects on the selective radiosensitization of prostate cells by GRPR-targeted gold nanoparticles. *Int J Mol Sci.* 2022;23(9):5279. doi:10.3390/ijms23095279
34. Li DD, Zhao J, Ma J, et al. GMT8 aptamer conjugated PEGylated Ag@Au core-shell nanoparticles as a novel radiosensitizer for targeted radiotherapy of glioma. *Colloids Surfaces B Biointer.* 2022;2022:211.
35. Kamalabadi MA, Neshastehriz A, Ghaznavi H, Amini SM. Folate functionalized gold-coated magnetic nanoparticles effect in combined electroporation and radiation treatment of HPV-positive oropharyngeal cancer. *Med Oncol.* 2022;39:12.
36. Guerra DB, Oliveira EMN, Sonntag AR, et al. Intercomparison of radiosensitization induced by gold and iron oxide nanoparticles in human glioblastoma cells irradiated by 6 MV photons. *Sci Rep.* 2022;12(1). doi:10.1038/s41598-022-13368-x
37. Goubault C, Jarry U, Bostoën M, et al. Radiosensitizing Fe-Au nanocapsules (hybridsomes (R)) increase survival of GL261 brain tumor-bearing mice treated by radiotherapy. *Nanomed Nanotechnol Biol Med.* 2022;2:40.
38. Li RT, Chen M, Yang ZC, et al. AIE-based gold nanostar-berberine dimer nanocomposites for PDT and PTT combination therapy toward breast cancer. *Nanoscale.* 2022;14(27):9818–9831. doi:10.1039/D2NR03408E
39. D'Acunto M, Cioni P, Gabellieri E, Presciuttini G. Exploiting gold nanoparticles for diagnosis and cancer treatments. *Nanotechnology.* 2021;32(19):192001. doi:10.1088/1361-6528/abe1ed
40. Riley RS, Day ES. Gold nanoparticle-mediated photothermal therapy: applications and opportunities for multimodal cancer treatment. *Wiley Interdiscip Rev Nanomed Nanobiotechnol.* 2017;9(4). doi:10.1002/wnan.1449
41. Gong LJ, Xie JN, Zhu S, Gu ZJ, Zhao YL. Application of multifunctional nanomaterials in tumor radiosensitization. *Acta Phys Chim Sin.* 2018;34(2):140–167.
42. Her S, Jaffray DA, Allen C. Gold nanoparticles for applications in cancer radiotherapy: mechanisms and recent advancements. *Adv Drug Deliv Rev.* 2017;109:84–101. doi:10.1016/j.addr.2015.12.012
43. Goswami N, Luo Z, Yuan X, Leong DT, Xie J. Engineering gold-based radiosensitizers for cancer radiotherapy. *Mater Horizons.* 2017;4(5):817–831. doi:10.1039/C7MH00451F
44. Li W, Brown PK, Wang LV, Xia Y. Gold nanocages as contrast agents for photoacoustic imaging. *Contrast Media Mol Image.* 2011;6(5):370–377. doi:10.1002/cmim.439
45. Li W, Chen X. Gold nanoparticles for photoacoustic imaging. *Nanomedicine.* 2015;10(2):299–320. doi:10.2217/nmm.14.169
46. Fan S, Zhang Y, Tan H, et al. Manganese/iron-based nanoprobe for photodynamic/chemotherapy combination therapy of tumor guided by multimodal imaging. *Nanoscale.* 2021;13(10):5383–5399. doi:10.1039/D0NR08831E
47. Liu Y, Yang J, Liu B, et al. Human iPSC cells loaded with MnO(2)-based nanoprobe for photodynamic and simultaneous enhanced immunotherapy against cancer. *Nanomicro Lett.* 2020;12(1):127. doi:10.1007/s40820-020-00452-y
48. Liu J, Gao J, Zhang A, et al. Carbon nanocage-based nanozyme as an endogenous H(2)O(2)-activated oxygenator for real-time bimodal imaging and enhanced phototherapy of esophageal cancer. *Nanoscale.* 2020;12(42):21674–21686. doi:10.1039/D0NR05945E

49. Cao W, Liu B, Xia F, et al. MnO(2)@Ce6-loaded mesenchymal stem cells as an “oxygen-laden guided-missile” for the enhanced photodynamic therapy on lung cancer. *Nanoscale*. 2020;12(5):3090–3102. doi:10.1039/C9NR07947E
50. Cui F, Liu J, Pang S, Li B. Recent advance in tumor microenvironment-based stimuli-responsive nanoscale drug delivery and imaging platform. *Front Pharmacol*. 2022;13:929854. doi:10.3389/fphar.2022.929854
51. Yang G, Ji J, Liu Z. Multifunctional MnO(2) nanoparticles for tumor microenvironment modulation and cancer therapy. *Wiley Interdiscip Rev Nanomed Nanobiotechnol*. 2021;13(6):e1720. doi:10.1002/wnan.1720
52. Liu Z, Zhang S, Lin H, et al. Theranostic 2D ultrathin MnO(2) nanosheets with fast responsibility to endogenous tumor microenvironment and exogenous NIR irradiation. *Biomaterials*. 2018;155:54–63. doi:10.1016/j.biomaterials.2017.11.015
53. Li X, Chen L, Luan S, et al. The development and progress of nanomedicine for esophageal cancer diagnosis and treatment. *Semin Cancer Biol*. 2022;86(Pt 2):873–885. doi:10.1016/j.semcancer.2022.01.007
54. Skrabalak SE, Au L, Li X, Xia Y. Facile synthesis of Ag nanocubes and Au nanocages. *Nat Protoc*. 2007;2(9):2182–2190. doi:10.1038/nprot.2007.326
55. Zhan C, Huang Y, Lin G, Huang S, Zeng F, Wu S. A gold nanocage/cluster hybrid structure for whole-body multispectral optoacoustic tomography imaging, EGFR inhibitor delivery, and photothermal therapy. *Small*. 2019;15(33):e1900309. doi:10.1002/smll.201900309
56. Liu Y, Pan Y, Cao W, et al. A tumor microenvironment responsive biodegradable CaCO(3)/MnO(2)- based nanoplatform for the enhanced photodynamic therapy and improved PD-L1 immunotherapy. *Theranostics*. 2019;9(23):6867–6884. doi:10.7150/thno.37586
57. Liu Y, Ai K, Liu J, Deng M, He Y, Lu L. Dopamine-melanin colloidal nanospheres: an efficient near-infrared photothermal therapeutic agent for in vivo cancer therapy. *Adv Mater*. 2013;25(9):1353–1359. doi:10.1002/adma.201204683
58. Zelepukin IV, Griaznova OY, Shevchenko KG, et al. Flash drug release from nanoparticles accumulated in the targeted blood vessels facilitates the tumour treatment. *Nat Commun*. 2022;13(1). doi:10.1038/s41467-022-34718-3

International Journal of Nanomedicine

Dovepress

Publish your work in this journal

The International Journal of Nanomedicine is an international, peer-reviewed journal focusing on the application of nanotechnology in diagnostics, therapeutics, and drug delivery systems throughout the biomedical field. This journal is indexed on PubMed Central, MedLine, CAS, SciSearch®, Current Contents®/Clinical Medicine, Journal Citation Reports/Science Edition, EMBase, Scopus and the Elsevier Bibliographic databases. The manuscript management system is completely online and includes a very quick and fair peer-review system, which is all easy to use. Visit <http://www.dovepress.com/testimonials.php> to read real quotes from published authors.

Submit your manuscript here: <https://www.dovepress.com/international-journal-of-nanomedicine-journal>